AGU PUBLICATIONS

Geophysical Research Letters

RESEARCH LETTER
10.1002/2017GL075661

Key Points:
- A new geothermal heat flux map of Greenland is obtained within ~15% accuracy using machine learning techniques
- The new map honors regional geology, tectonic settings, and ice core measurements
- Pockets of high heat flux are predicted in central-north Greenland and upstream of several fast-flowing outlet glaciers

Supporting Information:
- Supporting Information S1

Correspondence to:
S. Rezvanbehbahani,
soroushr@ku.edu

Citation:
Rezvanbehbahani, S., Stearns, L. A., Kadivar, A., Walker, J. D., and van der Veen, C. J. (2017). Predicting the geothermal heat flux in Greenland: A machine learning approach. *Geophysical Research Letters*, *44*, 12,271–12,279. https://doi.org/10.1002/2017GL075661

Received 12 SEP 2017
Accepted 14 NOV 2017
Accepted article online 16 NOV 2017
Published online 26 DEC 2017

Predicting the Geothermal Heat Flux in Greenland: A Machine Learning Approach

Soroush Rezvanbehbahani[1,2], Leigh A. Stearns[1,2], Amir Kadivar[3], J. Doug Walker[1], and C. J. van der Veen[4]

[1]Department of Geology, University of Kansas, Lawrence, KS, USA, [2]Center for Remote Sensing of Ice Sheets, University of Kansas, Lawrence, KS, USA, [3]Department of Mathematics and Statistics, McGill University, Montréal, Québec, Canada, [4]Department of Geography and Atmospheric Sciences, University of Kansas, Lawrence, KS, USA

Abstract Geothermal heat flux (GHF) is a crucial boundary condition for making accurate predictions of ice sheet mass loss, yet it is poorly known in Greenland due to inaccessibility of the bedrock. Here we use a machine learning algorithm on a large collection of relevant geologic features and global GHF measurements and produce a GHF map of Greenland that we argue is within ~15% accuracy. The main features of our predicted GHF map include a large region with high GHF in central-north Greenland surrounding the NorthGRIP ice core site, and hot spots in the Jakobshavn Isbræ catchment, upstream of Petermann Gletscher, and near the terminus of Nioghalvfjerdsfjorden glacier. Our model also captures the trajectory of Greenland movement over the Icelandic plume by predicting a stripe of elevated GHF in central-east Greenland. Finally, we show that our model can produce substantially more accurate predictions if additional measurements of GHF in Greenland are provided.

Plain Language Summary The heat generated at the interior regions of Earth (geothermal heat flux, GHF) can be high enough to melt the bottom layers of ice sheets, decrease friction between ice and bedrock, and increase ice discharge to the ocean. This heat, however, cannot be directly measured in ice sheets because the bedrock is inaccessible. Here we present a novel approach to estimate this heat. We combine all the available geologic, tectonic, and GHF data that are available on all continents. We then establish a complex relationship between GHF and all the geologic-tectonic features using machine learning techniques and then predict the GHF for the Greenland Ice Sheet. We utilize all information from available ice cores and bedrock boreholes to improve the GHF prediction in Greenland. Thus, the new GHF map honors tectonic settings, regional geology, and measurements from ice cores and can be used as an important input parameter to numerical ice sheet models that aim at lowering the uncertainties of future sea level rise predictions.

1. Introduction

Among the numerous input parameters needed to run ice sheet models, geothermal heat flux (GHF) is perhaps the least constrained by observations. GHF affects the ice temperature and viscosity, which can impact the ice sheet geometry and ice velocity (e.g., Larour et al., 2012; Pittard et al., 2016; Seroussi et al., 2017). In addition, the origin of ice streams in both Greenland and Antarctica is commonly associated with locally elevated heat flow in the underlying bedrock (e.g., Bell et al., 2007; Fahnestock et al., 2001). Therefore, it is critical to have a robust estimate of the spatial distribution of GHF in the underlying bedrock.

For the Greenland Ice Sheet (GrIS), the GHF is largely unknown apart from a few ice cores where GHF is inferred from the temperature gradient in the basal ice layers. Two GHF models are frequently used for Greenland: one inferred from seismic tomography (Shapiro & Ritzwoller, 2004) and the other from magnetic anomalies (Fox Maule et al., 2009). These two models differ significantly from each other and suffer from numerous simplifying assumptions and unknown parameters in ice-covered areas. Additionally, applying either of these GHF models in numerical ice sheet models cannot reproduce the observed temperatures at ice core locations (Rogozhina et al., 2012). Given the importance of GHF, it is clear that a new and independent estimate should be constructed that honors both the ice core data as well as Greenland geology.

This study derives a new map of GHF for the GrIS using statistical relationships between global heat flux observations and the combined influence of local geology and regional tectonic setting. Compilations of global

heat flux measurements on the continental crust include over 35,000 point measurements distributed across all continents. By assuming that GHF is a complex function of geologic and tectonic features (e.g., crustal thickness, magnetic anomaly, gravity field, rock type, age, elevation, and proximity to spreading ridge), we construct a machine learning algorithm to obtain the statistical relationship between geologic features and GHF. Based on the obtained relationship, we predict the GHF for Greenland and discuss the relative importance of input parameters in obtaining the new GHF map.

2. Data

2.1. GHF Measurements: Global Data Set

Global GHF data measured on the continents are obtained from the International Heat Flow Commission provided by the University of North Dakota (Gosnold, 2011). The data have a nearly normal and unimodal distribution, with mean and standard deviation of 60.8 and 18.2 mW m^{-2}, respectively (Figure S6 in the supporting information). The spatial resolution of the data varies considerably; North America and Europe are extensively surveyed, while measurements are sparse in South America and Africa. We use the mean of GHF values within each 1 by 1° latitude-longitude cell that reduces the number of points from 35,000 to more than 4,000 points. We apply a low-pass filter to remove the short-scale spatial variability and highlight the large-scale spatial patterns of GHF that we are interested in predicting for Greenland.

Prior to applying the low-pass filter, we limit our analysis to GHF values less than 200 mW m^{-2}, because even in Iceland (with an obvious mantle plume) the majority of heat flow measurements are below 200 mW m^{-2} (Hjartarson, 2015). Thus, we assume that for nonplume areas, such high readings are anomalous local processes (similar to Goutorbe et al., 2011) and are therefore removed to not contaminate our procedure.

2.2. GHF Measurements: Greenland

There are only 10 determinations of GHF in Greenland: five inferences from ice core sites and five direct bedrock measurements in ice-free coastal areas (Table S1 and Figure S7). GHF determinations at ice core sites usually mean that the GHF is inferred from the temperature gradient in the basal ice layer. GHF is also estimated using numerical ice sheet models by adjusting the GHF value at ice core locations so that the modeled basal temperature matches the measured basal temperature (e.g., Greve, 2005), or using a Monte Carlo simulation to inversely infer the GHF (e.g., Buchardt, 2009; Dahl-Jensen et al., 1998). Despite the uncertainties in these techniques, they form our current understanding of the GHF of the GrIS.

On the exposed rocks around the coast of Greenland, Sass et al. (1972) report GHF values of 37 and 41.8 mW m^{-2} in the southernmost part of Greenland. There is also one data point from Langseth et al. (1972) who measure the GHF at 51 mW m^{-2} in a fjord in south Greenland. In addition, the Greenland Analogue Project (GAP) reports two GHF measurements near Isunnguata Sermia in west Greenland of 27.2 mW m^{-2} (Meierbachtol et al., 2015) and 34.8 mW m^{-2} (Harper et al., 2011). Meierbachtol et al. (2015) do not report the exact location of their GHF measurements; therefore, we use the average GHF value of these measurements (because the study domain of Meierbachtol et al. (2015) is small, the two GHF measurements certainly fall in the same 1 by 1 latitude-longitude cell), which reduces the total number of GHF points in Greenland to nine.

2.3. Geologic Features

In contrast to other efforts to estimate GHF in Greenland that use single geophysical features such as gravity anomaly (Shapiro & Ritzwoller, 2004) or magnetic anomaly (Fox Maule et al., 2009), we use a compilation of geologic features and information that is globally available on the continental crust (Table 1). These geologic features are grouped into three major categories (similar to Goutorbe et al., 2011): (i) continuous data such as gravity anomaly and crustal thickness, (ii) categorical data including rock type and classes of velocity structure of the upper mantle, and (iii) proximity variables that describe the distance of each point to thermally active geologic features such as hot spots, ridges, and volcanoes. All geologic features are resampled to a 1° latitude-longitude grid using an ordinary kriging interpolation scheme.

3. Method

3.1. Overview of Statistical Models

The problem of predicting a continuous variable from a collection of relevant features is generally known as a regression problem. In our case, we wish to find a *predictor* that assigns a GHF value (denoted by $\widehat{\text{GHF}}$) to any point observation of geologic features. Performance of any such predictor is then evaluated by comparing its predictions to known GHF values. Such models are first *trained* on a set of point observations consisting of known values for geologic features and GHF, referred to as *training data*. The output of the training procedure

Table 1
Geologic Data Sets Included in the Feature Vector for Predicting GHF

Variable Type	Variable name	Reference
Continuous	Global surface topography	Amante and Eakins (2009)
	Greenland bedrock topography	Bamber et al. (2013)
	Depth to Moho	Reguzzoni et al. (2013)
	Lithosphere-asthenosphere boundary	Pasyanos et al. (2014)
	Age	Poupinet and Shapiro (2009)
	Bougeur gravity anomaly	Balmino et al. (2012)
	Crustal thickness	Laske et al. (2013)
	Upper mantle density anomaly	Kaban et al. (2004)
	Magnetic anomaly	Maus et al. (2007)
	Thickness of upper crust	Bassin (2000)
	Thickness of lower crust	Bassin (2000)
	Heat production provinces	Goutorbe et al. (2011)
Classification	Age of last thermotectonic event	USGS (1997)
	Upper Mantle velocity structure	Shapiro and Ritzwoller (2002)
	Rock type[a]	Hartmann and Moosdorf (2012)
	Rock type (Greenland)[a]	Dawes (2009)
Proximity	Distance to trench	Coffin et al. (1998) (UTIG Plates Project)
	Distance to transform ridge	Coffin et al. (1998) (UTIG Plates Project)
	Distance to young rift	Şengör and Natal'in (2001)
	Distance to volcano (5 nearest)	Goutorbe et al. (2011)
	Distance to ridge	Coffin et al. (1998) (UTIG Plates Project)
	Distance to hot spot	Caltech seismic lab (Anderson, 2016)

[a]The lithologies of Hartmann and Moosdorf (2012) and geologic provinces of Dawes (2009) are converted to the volcanic, sedimentary, and metamorphic rock types. Details are explained in the supporting information section 3 and Tables S2 and S3.

is an optimal predictor that minimizes prediction error with respect to some cost function. The main model we present here for GHF prediction is Gradient Boosted Regression Tree (GBRT, Friedman, 2001) that has many desirable properties including ability to discover nonlinear statistical relationships, as well as handling both continuous and categorical features in the regression model, and stability (Elith et al., 2008; Friedman et al., 2001) (see supporting information, section 1 for general explanation of GBRT and section 2.2 for our stability analysis of the model).

In order to assess the applicability of GBRT for GHF prediction, we compare its behavior to two simpler regression models. First, we consider a linear regression model that we subsequently show to be inferior to GBRT. Second, since applying constant GHF values to numerical ice sheet models is still common in glaciology, we include a "constant predictor" that simply predicts a spatially uniform GHF equal to the mean GHF value of its training data.

3.2. GHF Prediction Performance of GBRT

We use a standard cross-validation scheme in which the entire data set is randomly partitioned into two disjoint sets: a *training set* used to find the optimal GHF predictor and a *validation set* on which the optimal predictor is evaluated. To quantify prediction performance, we report two measures of error. First, we report the normalized root-mean-square error (RMSE) between predicted $\widehat{\mathrm{GHF}}$ and known GHF values in the validation set. Normalized RMSE is a standard and robust (invariant to rescaling) measure of error and is defined as

$$\text{Normalized RMSE} = \frac{1}{\langle \mathrm{GHF} \rangle} \sqrt{\left\langle \left| \mathrm{GHF} - \widehat{\mathrm{GHF}} \right|^2 \right\rangle},$$

where $\langle \cdot \rangle$ indicates the average over the validation set. Normalized RMSE can be interpreted as a relative measure of error; for instance, an error of 0.15 can be understood as an average 15% relative error in predictions.

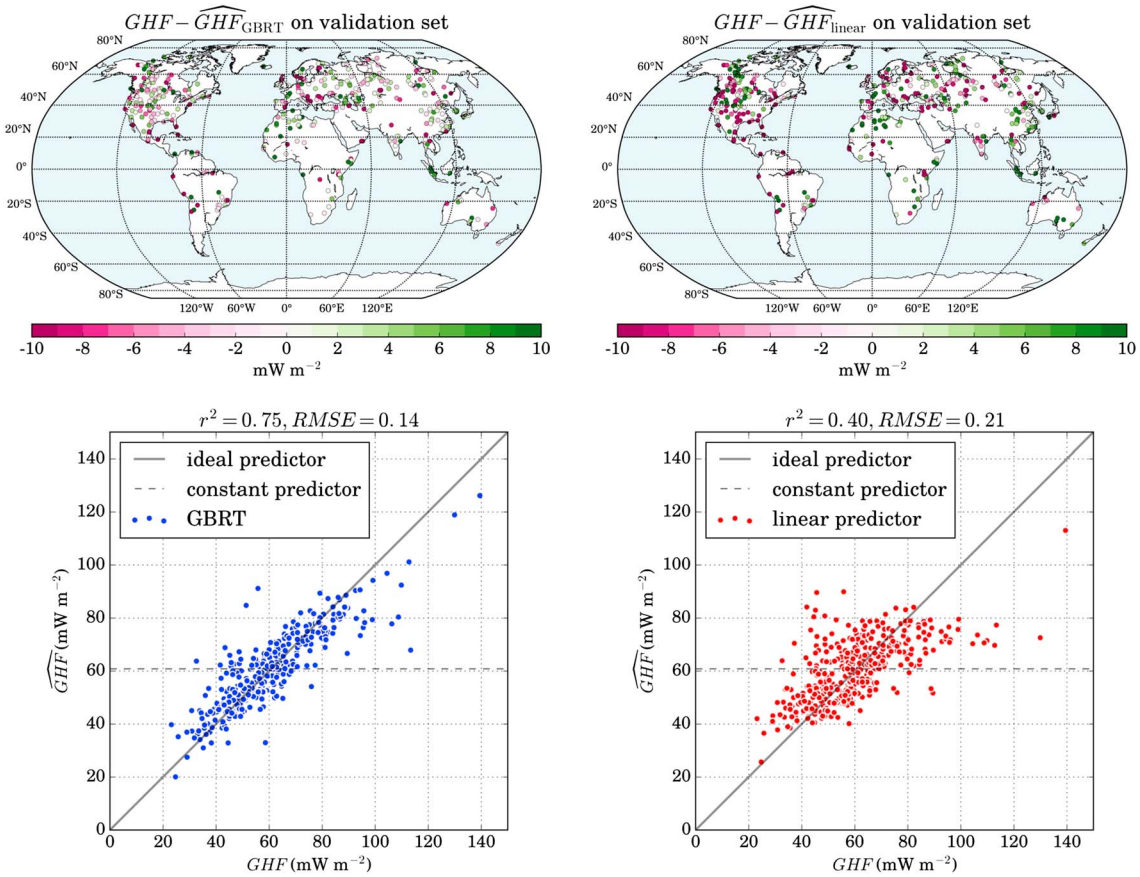

Figure 1. Performance of (left) GBRT and (right) linear regression when validation samples are distributed randomly. For each model, the difference between measurements and predictions (top) GHF − $\widehat{\mathrm{GHF}}$ and linear correlation analysis between (bottom) GHF and $\widehat{\mathrm{GHF}}$ is shown.

Second, we report the r^2 of linear correlation analysis between $\widehat{\mathrm{GHF}}$ and GHF on the validation set (see supporting information, section 2).

Using the above procedure with 80% of all data points for training and the remaining 20% for validation, GBRT predicts GHF with high accuracy (RMSE=0.14 and $r^2 = 0.75$), while predictions of the linear model have significantly higher error (RMSE=0.21 and $r^2 = 0.40$) as shown in Figure 1.

3.3. GHF Prediction With Limited Local Data

Since the goal of this work is to predict the heat flow specifically for Greenland, we investigate whether GBRT is capable of predicting GHF over a region with limited local data. We consider a region of interest (ROI) over which we wish to predict GHF. To quantify the abundance of local training data, we define the notion of *local training density* for an ROI as

$$\rho_{\mathrm{ROI}} = \frac{\text{no. of training samples in ROI}}{\text{area of ROI}}.$$

We then pose our question regarding GHF prediction with limited local data as follows: given a ρ_{ROI} and a radius R, what is the expected error in GHF prediction over an arbitrary circular ROI of radius R?

We answer the above question by modifying the cross-validation procedure described in the previous section. For a given ROI and a local training density ρ_{ROI} we randomly pick a subset of all available data points within the ROI as the local training set. These points together with all data points lying outside the ROI constitute the training set while the remaining samples within the ROI constitute the validation set (Figure 2). For each R and ρ_{ROI} we report the average value of normalized RMSE and r^2 over 50 random choices of ROI center in North America and west-central Europe; the choice of these regions is due to the large number of GHF measurements that are located in these regions (see supporting information, section 2).

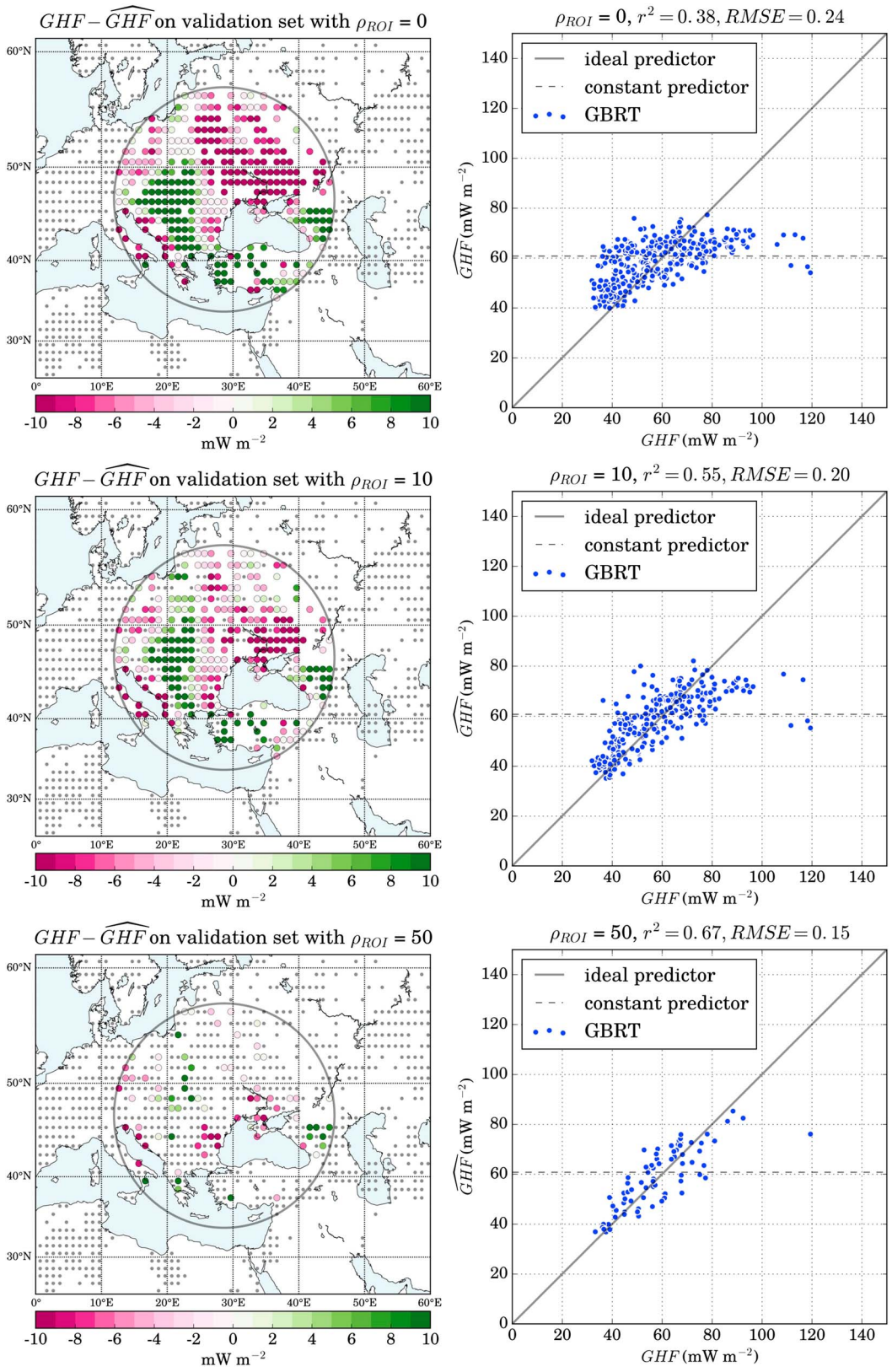

Figure 2. Step-wise improvement of GBRT predictions with increasing ρ_{ROI} shown over an arbitrary ROI of radius 1,300 km. In each map grey dots indicate training data, colored dots indicate validation points, and the grey circle is the ROI. For three densities (0, 10, and 50 per 10^6 km^2) the (right column) difference between measurements and predictions and (left column) their linear correlation is shown.

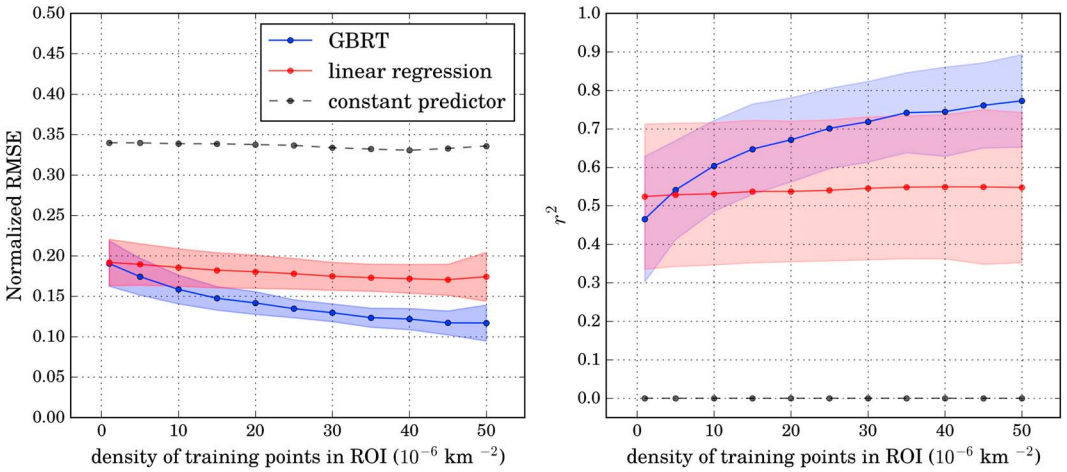

Figure 3. Normalized (left) RMSE and (right) r^2 of linear correlation, for GBRT (solid blue lines), linear regression (solid red lines), and constant predictor (dashed black lines) for different densities. For each model and density, the cross-validation procedure of Figure 2 is used and average errors on 50 ROIs of radius 1,300 km are reported. The blue and red regions show one standard deviation.

Using the above evaluation scheme, we find that regardless of the location of the circle, GHF predictions have high RMSE (~0.25) and low r^2 values (~0.4) when all samples from the ROI are excluded from the training set (i.e., $\rho_{\text{ROI}} = 0$). This shows that GBRT performs poorly over a region with no local training data (Figure 2, top row). If an area is completely removed from the training procedure, GBRT cannot spatially extrapolate and predict GHF over an ROI with no local training data, highlighting the importance of regional geology and tectonics in predicting GHF. Therefore, we investigate the extent to which this reduction in prediction performance relates to the density ρ_{ROI} of training samples within the ROI as well as the ROI radius R.

We run two sets of experiments for assessing the local performance of GBRT; corresponding results for linear regression and constant predictors are also included for comparison. In the first set of experiments we fix the ROI radius $R = 1,300$ km (size of Greenland) and vary ρ_{ROI} in each experiment from 5 to 50 samples per 10^6 km^2. Increasing ρ_{ROI} leads to lower RMSE and higher r^2 values for GBRT indicating increasing quality of prediction with increasing density of local training samples (Figures 2 and 3). Conversely, the linear model shows marginal reduction in RMSE and insignificant increase in r^2 with increasing ρ_{ROI} (Figure 3). We conduct similar procedures for North America and West Europe separately and find near-identical trends in RMSE and r^2 (as in Figure 3) that show that the model uncertainty does not depend on tectonic settings and local geology.

In the second set of experiments, we fix the local training density $\rho_{\text{ROI}} \sim 10$ per 10^6 km^2 (corresponding to the availability of training samples in Greenland, see section 3.4) and vary the radius, R, of the ROI from 500 to 4,000 km. Our results show that the RMSE of GBRT predictions remains unchanged with increasing values of R, while the corresponding r^2 continuously increases (Figure S3). In both sets of experiments, our results strongly confirm that GBRT performs significantly better than linear regression for predicting GHF with limited local data.

3.4. GHF Points for Greenland

There are only nine direct GHF measurements/inferences in Greenland; with $R = 1,300$ km, these measurements roughly constitute $\rho_{\text{ROI}} = 2$ per 10^6 km^2 on a 1 by 1° cell basis. With such sparse GHF measurements, our analysis shows that GBRT results in low r^2 values of 0.5 and RMSE of 0.2 (Figure 3). In order to compensate for the paucity of GHF points in Greenland, we assume that the regions surrounding each of the nine direct measurements in Greenland can be represented by a Gaussian kernel of the form $\text{GHF}_x = \text{GHF} * e^{-x^2/d^2}$ where GHF_x is the Gaussian-fit GHF at distance x from the ice core location. We assume an influence radius of 150 km for GHF near ice cores. For all GHF measurements in Greenland, we use the large value of $d = 1,000$ km that essentially results in a nearly planar distribution of GHF around the measurement location (e.g., ~2% decrease within 150 km radius for 30 mW m^{-2} measurement, Figure S7). The exception is at NorthGRIP ice core. Because the inferred GHF at NorthGRIP is anomalously high (Table S1), we assume the high GHF is a very local process (see section 2.1), and thus, we chose $d = 200$ km for the Gaussian kernel to make GHF drop more rapidly from high GHF values. By fitting the Gaussian kernel around ice cores, we increase the number of known GHF values

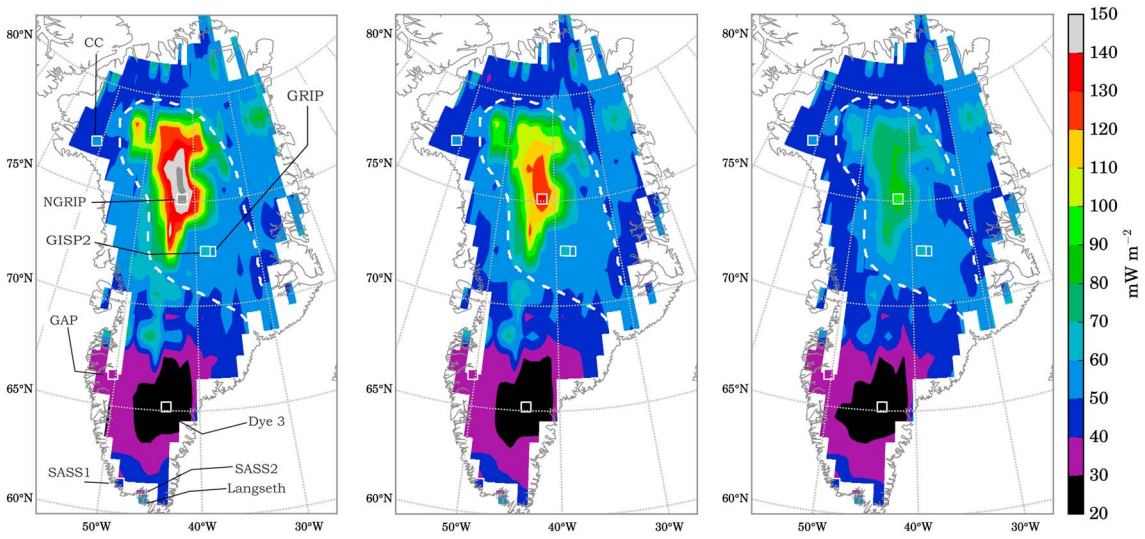

Figure 4. GHF predictions of GBRT for Greenland. Direct GHF measurements from the coastal rock cores, inferences from ice cores, and additional Gaussian-fit GHF data around ice core sites are used as training samples within the ROI leading to ρ_{ROI} = 11.3 per 10^6 km^2. Predictions are shown for three different values prescribed at NorthGRIP: (left) 160 mW m^{-2} as the upper limit (Dahl-Jensen et al., 2003), (middle) 135 mW m^{-2} suggested by Greve (2005), and (right) 90 mW m^{-2} as the lower range suggested by Dahl-Jensen et al. (2003). The white dashed region roughly shows the extent of elevated heat flux and a possible trajectory of Greenland's movement over the Icelandic plume.

in Greenland from 9 to more than 60, which is equivalent to ρ_{ROI}=11.3 per 10^6 km^2 for R = 1, 300 km. Based on the performance analysis shown in Figure 3, our GHF prediction for Greenland is expected to be within 15% of correct values (RMSE=0.15, r^2 = 0.6).

4. Results and Discussion

4.1. GHF Prediction for Greenland

In order to train GBRT for predicting the GHF in Greenland, we include the entire global GHF data set in addition to the points that we add for Greenland using the Gaussian kernel (Figure S7). We perform the prediction for Greenland using three GHF values at the NorthGRIP ice core: Dahl-Jensen et al. (2003) estimate an upper and lower bounds of 160 and 90 mW m^{-2}, respectively, based on modeling the age of ice layers in radar echograms, and Greve (2005) calculates that the GHF of 135 mW m^{-2} is the GHF required to match the measured and modeled basal melt rate at the NorthGRIP site. The GHF predictions using these three GHF values at NorthGRIP are shown in Figure 4.

The predictions show that apart from the anomalously high heat flux near the NorthGRIP ice core, a relatively large northern region that spreads from the interior east and west has a similarly high GHF value. Changing the magnitude of the prescribed GHF at the NorthGRIP ice core location alters the magnitude of predicted GHF in this region, but the spatial pattern and extent remain unchanged.

Our model predicts a region with relatively low GHF in south Greenland, which is consistent with the GHF measurements and age of the North Atlantic Craton. The extent of this low heat flux region (GHF values less than 40 mW m^{-2}) corresponds well with the suggested extent of the North Atlantic Craton (Dawes, 2009, Figure 1). In addition, GHF measurements across the Labrador Sea, on the Canadian region of the North Atlantic Craton show low GHF values of about 25 mW m^{-2}, comparable to our predictions in south Greenland (Mareschal & Jaupart, 2004; Figure 4).

There are a number of distinguishable features in our predicted GHF map. First is the slightly elevated predicted GHF that forms a path from northwest to central-east Greenland (white dashed line in Figure 4). This path closely follows the span of Icelandic plume tracks suggested by Rogozhina et al., 2016 (2016, Figure S8). Other notable features are the two pockets of high GHF in central-west Greenland, which persist regardless of the choice of GHF for NorthGRIP. This region is at the center of the catchment that is drained by Jakobshavn Isbræ. It is important to note that there are no GHF measurements/observations in this region. The closest GHF measurement is the location of the GAP project (Harper et al., 2011) that has a low GHF of 30 mW m^{-2}. Similar regions of elevated GHF exist in the northeast region, close to the margin of the ice sheet, near the

terminus of Nioghalvfjerdsfjorden (79North). There is no nearby GHF measurement in this region either, and therefore, these predictions are independent of the prescribed GHF values in Greenland.

4.2. Interpretation of GBRT Predictions

A standard technique in probing additive models is to first take the total amount of reduction in prediction error provided by each feature as its importance in an individual tree. Then the average error reduction over all trees provides a relative measure of importance for each feature (see supporting information section 3.1). Our model predicts topography, distance to young rifts, distance to trench, depth of lithosphere-asthenosphere boundary, and depth to Moho as the top five important features, respectively (Figure S5).

The relative importance of the top 10 features are very close to each other that hinders a straightforward association of the observed GHF patterns to individual geologic features. Furthermore, summarizing the importance of each feature in a single number will mask the importance of features that are somehow correlated with each other. In our feature vector, for example, distance to volcanoes is likely correlated with distance to hot spots and rifts. Including strongly correlated features in the feature vector only marginally improves the model performance, but the relative importance of correlated features will get distributed (Figure S5). A robust interpretation or simplification of the GBRT model presented here is beyond the scope of current study and is a potential avenue for future work (see supporting information, section 3.2).

5. Conclusion

Using the Gradient Boosted Regression Tree (GBRT) algorithm, we present a robust statistical relationship between a large group of geologic and tectonic features and global GHF. We combine the global GHF measurements on the continental crust with GHF inferences from ice cores, and few available GHF measurements on exposed coastal rock in Greenland and train GBRT to predict the GHF for the entire unsurveyed land mass of Greenland.

Our predicted GHF map shows a notable contrast between the regions south and north of ~67° with south having significantly lower GHF than north. The GHF map predicts a large region with high GHF in central-north Greenland close to the NorthGRIP ice core site, where other studies suggest thin lithosphere and trajectory of crust movement over the Icelandic plume as the cause of elevated GHF. This trajectory is also captured by our model in central-east Greenland. Finally, our GHF map shows slightly elevated GHF in central-west Greenland (upstream of Jakobshavn Isbræ), near the terminus of Nioghalvfjerdsfjorden in northwest, and small pockets in the northern regions.

The model's performance evaluation shows that the performance of GBRT will be significantly improved if any additional GHF measurements become available in Greenland and thus resolve the need for logistically expensive field measurements for the entire ice sheet.

Acknowledgments

The authors wish to thank scientific editor and an anonymous referee whose comments substantially helped clarify the manuscript. We also wish to thank Siavosh R. Behbahani for insightful comments and helping with analyzing the results. J. D. W. acknowledges the NSF award ICER: 1639734. The codes and data used in this study are publicly available through https://github.com/amirkdv/ghf-greenland-gbrt.

References

Amante, C., & Eakins, B. W. (2009). *ETOPO1 1 arc-minute global relief model: Procedures, data sources and analysis*. U.S. Department of Commerce, National Oceanic and Atmospheric Administration, National Environmental Satellite, Data, and Information Service, National Geophysical Data Center, Marine Geology and Geophysics Division Colorado.

Anderson, D. L. (2016). The complete hot spot. Retrieved from http://www.mantleplumes.org/CompleateHotspot. html, Accessed 08-29-2016.

Balmino, G., Vales, N., Bonvalot, S., & Briais, A. (2012). Spherical harmonic modelling to ultra-high degree of Bouguer and isostatic anomalies. *Journal of Geodesy*, *86*(7), 499–520.

Bamber, J. L., Griggs, J. A., Hurkmans, R., Dowdeswell, J. A., Gogineni, S. P., Howat, I., … Steinhage, D. (2013). A new bed elevation dataset for Greenland. *The Cryosphere*, *7*(2), 499–510.

Bassin, C. (2000). The current limits of resolution for surface wave tomography in North America. *Eos Transactions American Geophysical Union*, *81*, F897.

Bell, R. E., Studinger, M., Shuman, C. A., Fahnestock, M. A., & Joughin, I. (2007). Large subglacial lakes in East Antarctica at the onset of fast-flowing ice streams. *Nature*, *445*(7130), 904–907.

Buchardt, S. L. (2009). Basal melting and Eemian ice along the main ice ridge in Northern Greenland (PhD thesis). Copenhagen, Denmark: University Copenhagen.

Coffin, M. F., Gahagan, L. M., & Lawver, L. A. (1998). Present-day plate boundary digital data compilation. *University of Texas Institute for Geophysics Technical Report*, *174*, 5.

Dahl-Jensen, D., Gundestrup, N., Gogineni, S. P., & Miller, H. (2003). Basal melt at NorthGRIP modeled from borehole, ice-core and radio-echo sounder observations. *Annals of Glaciology*, *37*(1), 207–212.

Dahl-Jensen, D., Mosegaard, K., Gundestrup, N., Clow, G. D., Johnsen, S. J., Hansen, A. W., & Balling, N. (1998). Past temperatures directly from the Greenland ice sheet. *Science*, *282*(5387), 268–271.

Dawes, P. R. (2009). The bedrock geology under the inland ice: The next major challenge for Greenland mapping. *Geological Survey of Denmark and Greenland Bulletin*, *17*(5), 57–60.

Elith, J., Leathwick, J. R., & Hastie, T. (2008). A working guide to boosted regression trees. *Journal of Animal Ecology*, *77*(4), 802–813.
Fahnestock, M., Abdalati, W., Joughin, I., Brozena, J., & Gogineni, P. (2001). High geothermal heat flow, basal melt, and the origin of rapid ice flow in central Greenland. *Science*, *294*(5550), 2338–2342.
Fox Maule, C., Purucker, M. E., & Olsen, N. (2009). Inferring magnetic crustal thickness and geothermal heat flux from crustal magnetic field models (Danish Climate Centre Report 09–09, 33 pp.). Danish Meteorological Institute.
Friedman, J., Hastie, T., & Tibshirani, R. (2001). *The elements of statistical learning* (Vol. 1). Berlin: Springer series in statistics Springer.
Friedman, J. H. (2001). Greedy function approximation: A gradient boosting machine. *Annals of statistics*, *29*, 1189–1232.
Gosnold, W. (2011). The global heat flow database. Retrieved from http://www.heatflow.und.edu/index2.html. (Accessed: 09-30-2016).
Goutorbe, B., Poort, J., Lucazeau, F., & Raillard, S. (2011). Global heat flow trends resolved from multiple geological and geophysical proxies. *Geophysical Journal International*, *187*(3), 1405–1419.
Greve, R. (2005). Relation of measured basal temperatures and the spatial distribution of the geothermal heat flux for the Greenland ice sheet. *Annals of Glaciology*, *42*(1), 424–432.
Harper, J., Hubbard, A., & Ruskeeniemi, T. (2011). The Greenland analogue project. Yearly report 2010 (Technical Report). Swedish Nuclear Fuel and Waste Management Co.
Hartmann, J., & Moosdorf, N. (2012). The new global lithological map database GLiM: A representation of rock properties at the Earth surface. *Geochemistry, Geophysics, Geosystems*, *13*, Q12004. https://doi.org/10.1029/2012GC004370
Hjartarson, Á. (2015). Heat flow in Iceland. In *Proceedings World Geothermal Congress*. Melbourne, Australia.
Kaban, M. K., Schwintzer, P., & Reigber, C. (2004). A new isostatic model of the lithosphere and gravity field. *Journal of Geodesy*, *78*(6), 368–385.
Langseth, M. G., Clark Jr, S. P., Chute Jr, J. L., Keihm, S. J., & Wechsler, A. E. (1972). Heat flow experiment (Apollo 15 Preliminary Science Report). Washington, DC: NASA SP-330.
Larour, E., Morlighem, M., Seroussi, H., Schiermeier, J., & Rignot, E. (2012). Ice flow sensitivity to geothermal heat flux of Pine Island Glacier, Antarctica. *Journal of Geophysical Research*, *117*, F04023. https://doi.org/10.1029/2012JF002371
Laske, G., Masters, G., Ma, Z., & Pasyanos, M. (2013). Update on CRUST1.0 1-degree global model of EarthŠs crust. *Geophysical Research Abstracts*, *15*, 2658.
Mareschal, J. C., & Jaupart, C. (2004). Variations of surface heat flow and lithospheric thermal structure beneath the North American craton. *Earth and Planetary Science Letters*, *223*(1), 65–77.
Maus, S., Sazonova, T., Hemant, K., Fairhead, J. D., & Ravat, D. (2007). National geophysical data center candidate for the world digital magnetic anomaly map. *Geochemistry, Geophysics, Geosystems*, *8*, Q06017. https://doi.org/10.1029/2007GC001643
Meierbachtol, T. W., Harper, J. T., Johnson, J. V., Humphrey, N. F., & Brinkerhoff, D. J. (2015). Thermal boundary conditions on western Greenland: Observational constraints and impacts on the modeled thermomechanical state. *Journal of Geophysical Research: Earth Surface*, *120*, 623–636. https://doi.org/10.1002/2014JF003375
Pasyanos, M. E., Masters, TG., Laske, G., & Ma, Z. (2014). LITHO1.0: An updated crust and lithospheric model of the Earth. *Journal of Geophysical Research: Solid Earth*, *119*, 2153–2173. https://doi.org/10.1002/2013JB010626
Pittard, M. L., Galton-Fenzi, B. K., Roberts, J. L., & Watson, C. S. (2016). Organization of ice flow by localized regions of elevated geothermal heat flux. *Geophysical Research Letters*, *43*, 3342–3350. https://doi.org/10.1002/2016GL068436
Poupinet, G., & Shapiro, N. M. (2009). Worldwide distribution of ages of the continental lithosphere derived from a global seismic tomographic model. *Lithos*, *109*(1), 125–130.
Reguzzoni, M., Sampietro, D., & Sansò, F. (2013). Global Moho from the combination of the CRUST2.0 model and GOCE data. *Geophysical Journal International*, *195*, 222–237.
Rogozhina, I., Hagedoorn, J. M., Martinec, Z., Fleming, K., Soucek, O., Greve, R., & Thomas, M. (2012). Effects of uncertainties in the geothermal heat flux distribution on the Greenland ice sheet: An assessment of existing heat flow models. *Journal of Geophysical Research*, *117*, F02025. https://doi.org/10.1029/2011JF002098
Rogozhina, I., Petrunin, A. G., Vaughan, A. P. M., Steinberger, B., Johnson, J. V., Kaban, M. K., … Koulakov, I. (2016). Melting at the base of the Greenland ice sheet explained by Iceland hotspot history. *Nature Geoscience*, *9*(5), 366–369.
Sass, J. H., Nielsen, B. L., Wollenberg, H. A., & Munroe, R. J. (1972). Heat flow and surface radioactivity at two sites in South Greenland. *Journal of Geophysical Research*, *77*(32), 6435–6444.
Şengör, A. C., & Natal'in, B. A. (2001). Rifts of the world. *Geological Society of America Special Papers*, *352*, 389–482.
Seroussi, H., Ivins, E. R., Wiens, D. A., & Bondzio, J. (2017). Influence of a west Antarctic mantle plume on ice sheet basal conditions. *Journal of Geophysical Research: Solid Earth*, *122*, 7127–7155. https://doi.org/10.1002/2017JB014423
Shapiro, N. M., & Ritzwoller, M. H. (2002). Monte-Carlo inversion for a global shear-velocity model of the crust and upper mantle. *Geophysical Journal International*, *151*(1), 88–105.
Shapiro, N. M., & Ritzwoller, M. H. (2004). Inferring surface heat flux distributions guided by a global seismic model: Particular application to Antarctica. *Earth and Planetary Science Letters*, *223*(1), 213–224.
USGS (1997). Geologic province and thermo-tectonic age maps. Retrieved from https://earthquake.usgs.gov/data/crust/maps.php. (Accessed 09-30-2016).